Green Fabrication of Polyimide Fibers with Phosphate Monoester Network to Reinforce Carbon Nanotube Polymer Composites: Simultaneously improving the Mechanical Properties and Flame Retardancy

Hongyang Dang[1] · Yunfeng Cao[2] · Ruqiang Zhang[1] · Zhu Long[1,3] · Shuai Guo[3] · Shihua Wang[3,4] · Zhiqiang Li[3,4]

Abstract

To further enhance the reinforcing effect of polyimide (PI) fibers on carbon nanotube polymer composites, in this work, networks of long chains of phosphate monoester (PMOEs) were grown on the surface of PI fibers, and silanized multiwalled carbon nanotubes (Si-MWCNTs) were dispersed into the phenolic resin (PR) matrix. Subsequently, these two interpenetrating networks were entangled tightly at the PI-PMOEs fiber paper/ PR matrix by vacuum-assisted wet papermaking technology and impregnation and vacuum curing technology. A novel type of PI-PMOEs fiber-reinforced carbon nanotube polymer composite was prepared. Structural observation and analysis revealed that the fiber surface activity and roughness were improved, resulting in enhanced interfacial adhesion. The Si-MWCNTs at the interface play an anchoring role, which leads to a strong mechanical interlock between the PI-PMOEs fibers and the matrix. Therefore, the generation and propagation of cracks encountered greater resistance, and the mechanical properties of the composites were improved. Compared with the Si-MWCNTs/PR composite with tensile strength of 20.29 MPa and elongation at break of 0.1%, the tensile strength and elongation at break of 80PI-PMOEs/Si-MWCNTs/PR (the basis weight of paper is 40 wt.%) composite are increased to 91.22 MPa and 2.0%, respectively. In addition, a tightly connected fiber "large skeleton" was provided by the PI-PMOEs fiber paper with a uniform pore size distribution. The Si-MWCNTs network and the thermally degraded carbides of the matrix formed a "small skeleton" based on the "large skeleton", resulting in a complete and dense protective barrier layer. The volatilization of pyrolysis products (CO, small-molecule hydrocarbons, aromatic compounds, etc.) was restricted, and heat and mass transfer were suppressed. Finally, the composites exhibited excellent flame retardancy.

Keywords Polyimide fiber · Enzyme catalysis · Carbon nanotube polymer composites · Mechanical properties · Flame retardancy

✉ Zhu Long
  longzhu@jiangnan.edu.cn

Extended author information available on the last page of the article

1 Introduction

In recent years, carbon nanotube (CNT) polymer composites have been the focus of attention of researchers [1–5]. Compared with traditional reinforcements, the addition of nano-level materials such as CNTs can effectively improve the internal stress transmission of the composites. Moreover, well-dispersed CNTs will form bridges, which will hinder heat transfer. Even a small amount of additives can significantly improve the properties of the polymer matrix [6–8]. In addition, the interphase regions are commonly formed in polymer nanocomposites, due to the outstanding surface area of nanoparticles and strong interfacial adhesion between matrix and filler phases [9–14]. And the interphase region can significantly enhance the properties of nanocomposites.

However, CNTs have large aspect ratios and specific surface areas, resulting in the formation of many aggregates in the polymer matrix due to van der Waals forces [15, 16]. When the composite is loaded, the aggregated CNT particles cause a concentration of stress on the crack propagation surface [17]. In the process of composite combustion, uniformly dispersed CNTs can act as bridges between the flame retardant fillers in the polymer matrix and help to inhibit thermal degradation [18, 19]. Therefore, it is necessary to improve the dispersibility of CNTs and the interfacial compatibility between CNTs and the polymer matrix, which helps to enhance the properties of carbon nanotube polymer composites. Gkikas et al. processed CNTs and an epoxy matrix by ultrasonic treatment, and they found that the fracture toughness of the composite increased approximately 50% when the CNT treatment time was 1 h [20]. Zhang et al. prepared MWCNTs with amino and acyl chloride groups on the surface by chemical functionalization, and the mechanical properties of the MWCNT-reinforced epoxy composite were improved [21]. Wang et al. enhanced the properties of a two-dimensional molybdenum disulfide (MoS_2)/epoxy composite with the help of an MWCNT nano bridge. It was found that the MWCNTs were well dispersed in the matrix under the synergistic effect of mixed acid and ultrasonic treatment, and the tensile strength of the composite was improved. Furthermore, the dense barrier network composed of MWCNTs and MoS_2 nanosheets inhibited the pyrolysis reaction and further hindered the combustion process [22]. It can be found from the above studies that a flexible combination of different dispersion methods can play a better role in synergy and further enhance the properties of composites.

The increase in CNT surface activity can improve its dispersibility and compatibility between two phases, which is helpful for preparing high-performance composites. It is undeniable that the effective length of CNT is limited, and the network formed in the matrix is unstable. Consequently, high-strength and high-modulus organic synthetic fibers are considered better candidates for reinforced CNT polymer composites. Micheli et al. investigated a multifunctional composite composed of an aramid fiber fabric and epoxy matrix containing CNTs and found that an aramid fabric layer with a thickness of 3.5 mm can effectively resist and absorb energy at a speed of 400 m/s and a strength of 600 J, and at least provide a shielding effect with a frequency of 80 dB [23]. Ahmadi et al. used ultra-high molecular weight polyethylene (UHMWPE) fibers grafted with unidirectional glycidyl methacrylate (GMA) to reinforce an epoxy resin dispersed with carbon nanofibers (CNFs). They found that the combined use of CNFs and GMA-grafted UHMWPE fibers leads to significant synergy in the mechanical properties of nanocomposites. In particular, the UHMWPE fibers play a leading role in improving the bending strength of composites [24]. In conclusion, the introduction

of high-performance organic synthetic fibers results in composite materials with higher mechanical strength and other properties, thereby improving their competitiveness in application fields.

Polyimide (PI) fiber is a new member of the family of synthetic fibers, and it has been widely used in the aerospace, military, automotive and construction industries in recent years [25–27]. PI fiber is an ordered linear polymer formed by a benzene ring, five-membered heterocyclic ring, imide ring, carboxyl group, and other structural units [28, 29]. PI fibers exhibit outstanding thermal stability, prominent mechanical properties, excellent electrical insulation and low dielectric performance due to their unique aramid molecular structure [30–34]. However, PI fiber has more inert groups and smaller specific surface areas, leading to weak interface affinity and difficulty in uniform dispersion in the polymer matrix. The enhancement of the properties of CNT polymer composites by PI fibers is greatly hindered [35–37]. Therefore, it is necessary to simultaneously improve the interfacial compatibility between the fibers and the polymer matrix and the dispersibility of the fibers in the matrix.

In the present work, we chose green horseradish peroxidase (HRP) as a high-efficiency catalyst, and phosphate monoester (PMOE) with polyhydroxy groups was grown on the surface of PI fibers in an inverse microemulsion environment by free-radical polymerization. The surface activity and hydrophilicity of the fiber were improved, and the loss of its excellent properties decreased. Then, a PI-PMOEs fiber paper precursor with a uniform pore size distribution was prepared by means of vacuum-assisted wet papermaking technology. In addition, Si-MWCNTs were dispersed in a PR matrix/ethanol solution by high-frequency ultrasound, and the mixture was used for the impregnation of fiber paper precursors. Finally, PI-PMOEs fiber-reinforced Si-MWCNT/PR composites were prepared by vacuum curing technology. Additionally, the reinforcing results and factors influencing the mechanical properties and flame retardancy of the composites upon introduction of PI-PMOEs fibers were investigated. Finally, the electrical property of composites was determined. The purpose of this study was to prepare PI fibers with better hydrophilicity by an eco-friendly and less destructive processing method. Moreover, a novel technology was developed to prepare organic fiber-reinforced carbon nanotube polymer composites with good mechanical properties and flame retardancy. Broad application prospects in fiber-reinforced carbon nanotube polymer composites can be expected in future engineering, especially in the field of fire-resistant composites.

2 Experimental

2.1 Materials

PI fiber (length = 3 mm, diameter = 11.28 μm, density = 1.41 g/cm^3, strength = 4.38 GPa, elongation at break = 5.0%) was kindly supplied by Aoshen New Material Co., Ltd. (Lianyungang, China). Aramid pulp (XGJP1201, density = 1.47 g/cm^3, length = 0.3-0.6 mm, breaking strength = 1.94 GPa) was purchased from Dupont China Holding Co., Ltd. (Shanghai, China). Graphitized multiwalled carbon nanotubes (MWCNTs, HQNANO-CNTs-008-4H) were purchased Tanfeng Graphene Technology Co., Ltd. (Suzhou, China), and the carboxyl group content of the MWCNTs was 0.36 wt.% (length = 10-30 μm, inner diameter = 5-15 nm, outer diameter > 50 nm). Thermosetting phenolic resin (PR, 2123-A, free phenol content ≤ 1.5 wt.%) was purchased from Chengfeng Resin Industry Co.,

Ltd. (Xingtai, China). Phosphate-buffered saline (PBS, pH = 6.9) was purchased from Haibiao Technology Co., Ltd. (Xiamen, China). Horseradish peroxidase (HRP, activity $\geq$ 250 U/mg) was purchased from Dulai Biotechnology Co., Ltd. (Nanjing, China). N-Dode-cyltrimethylsilane (DBS, $\geq$ 96%) was purchased from Hongming Chemical Reagent Co., Ltd. (Jining, China). All other reagents—including hydroxyethyl methacrylate (HEMA, $\geq$ 96%), phosphorus pentoxide (P_2O_5, AR), hydroquinone (HQ, AR), n-butanol (NBA, AR), n-octane (C_8H_{18}, AR), sodium dodecylbenzene sulfonate (LAS, AR), 1,4-dioxane (Diox, AR), sodium percarbonate (SPC, $\geq$ 98%), acetone (CH_3COCH_3, AR), ethanol (C_2H_6O, AR), sulfuric acid (H_2SO_4, AR) and nitric acid (HNO_3, AR)—were provided by Sinop-harm Chemical Reagent Co., Ltd. (Shanghai, China). Deionized water was prepared in the laboratory. All chemicals and materials were used as received without further purification. Ethanol (γ^d = 23.00 mJ/m^2, γ^p = 19.00 mJ/m^2) and deionized water (γ^d = 21.80 mJ/m^2, γ^p = 51.00 mJ/m^2) were used as fiber contact angle experimental liquids.

2.2 Preparation of PI Fiber with Surface-Grown PMOEs Network

To remove the organic impurities from the surface of pristine PI fibers, the pristine PI fib-ers were treated ultrasonically (200 W, DS-1000Y, Dusi Instrument Co., Ltd., China) in acetone solution for 1 h and then dried at 60°C. The resulting fibers were denoted as PI.

Construction of the inverse (W/O) microemulsion system: Approximately 9 mL n-octane was used as the oil phase, and 6 g LAS and 3 mL n-butanol were added as the emulsifier and co-emulsifier, respectively. Finally, 23.4 mL PBS (0.1 M) was added as the aqueous phase. After slight shaking and stirring with a glass rod, a transparent and clear inverse microemulsion was prepared.

Approximately 0.3 g PI fiber bundles, 64.8 mL Diox, 8 mL PBS containing 2 mg HRP, and 12.8 g PMOE (10 mL, see the synthetic process in Section I of the Supporting Infor-mation) were successively added to a three-necked flask equipped with a thermometer and condensation reflux device. After the mixture was degassed for 1 h, approximately 0.45 g SPC was added to the flask in batches for more than 1 h. Next, the temperature was held at 70°C for 14 h under continuous stirring. Consequently, the fibers were refluxed in a mix-ture of deionized water and acetone for 24 h and finally dried at 80°C. The resultant fiber was denoted as PI-PMOEs-1. Furthermore, PI-PMOEs-2 and PI-PMOEs-3 were prepared under the above conditions, and the amounts of PMOE were 19.2 g (15 mL) and 25.6 g (20 mL), respectively.

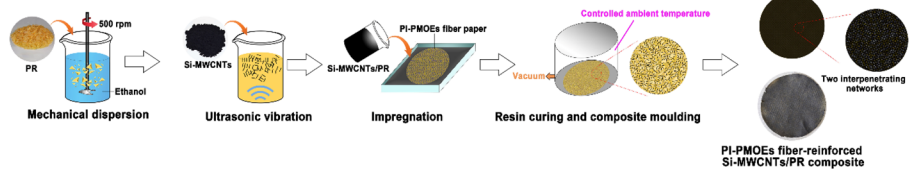## 2.3 Fabrication of PI-PMOEs Fiber-Reinforced Si-MWCNTs/PR Composites

The PI-PMOEs-3 fibers were selected as composite reinforcements and assigned as PI-PMOEs. Scheme 1 describes the fabrication process of fiber-reinforced Si-MWCNTs/PR composites. The PI-PMOEs fibers and aramid pulp were dispersed in a vertical standard fiber disintegrator (3000 rpm, PL28-2, Xianyang Taisite Test Equipment Co., Ltd., China) at a mass ratio of 7:3 for 15 min. Next, the fiber suspension was poured into a paper former (ZQJ1-B-II; Shaanxi University of Science and Technology Machinery Factory, China), and the PI-PMOEs fiber paper precursor with a basis weight of 50 g/m^2 was prepared by vacuum filtration and squeezing.

The procedure for preparing PI-PMOEs fiber paper-reinforced Si-MWCNTs/PR composites is as follows: i) Approximately 60 g PR fragments were dissolved in etha-nol solution by mechanical agitation. ii) Then, approximately 0.4 g Si-MWCNTs (see

(a) Vacuum-assisted wet papermaking process
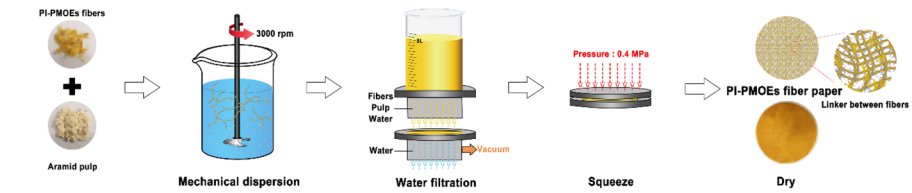
(b) Impregnation and vacuum curing process

Scheme 1. Schematic illustration for the preparation of PI-PMOEs fiber-reinforced Si-MWCNTs/PR composites: (**a**) vacuum-assisted wet papermaking, (**b**) impregnation and vacuum curing.

the silanization process in Section II of the Supporting Information) were uniformly dispersed in the above PR/ethanol solution by ultrasonic vibration for 30 min. iii) Afterwards, the PI-PMOEs fiber paper was immersed in a stainless steel container (25 cm × 25 cm × 5 cm) containing the above mixture for 5 min. iv) Finally, resin curing and composite moulding processes of the impregnated fiber paper were carried out in a temperature-controlled vacuum environment. The curing scheme was maintained for 1 h at 80℃, 4 h at 120℃ and 2 h at 150℃. The fiber content in the polymer composites was controlled by changing the concentration of the impregnation mixture.

Furthermore, neat Si-MWCNTs/PR polymer composites without fibers were prepared in a polytetrafluoroethylene mould by using the above raw material ratio and curing scheme. All the details of the formulation are listed in Table 1.

Table 1. Formulation of the Si-MWCNTs/PR and its composites

Specimen	Components	
	Si-MWCNTs/ PR (wt.%)	Fiber paper (wt.%)
Si-MWCNTs/PR	100	0
50g/m^2 PI fiber paper/Si-MWCNTs/PR (50PI/Si-MWCNTs/PR)	75	25
60g/m^2 PI fiber paper/Si-MWCNTs/PR (50PI/Si-MWCNTs/PR)	70	30
70g/m^2 PI fiber paper/Si-MWCNTs/PR (50PI/Si-MWCNTs/PR)	65	35
80g/m^2 PI fiber paper/Si-MWCNTs/PR (50PI/Si-MWCNTs/PR)	60	40
50g/m^2 PI-PMOEs fiber paper/Si-MWCNTs/PR (50PI-PMOEs/Si-MWCNTs/PR)	75	25
60g/m^2 PI-PMOEs fiber paper/Si-MWCNTs/PR (50PI-PMOEs/Si-MWCNTs/PR)	70	30
70g/m^2 PI-PMOEs fiber paper/Si-MWCNTs/PR (50PI-PMOEs/Si-MWCNTs/PR)	65	35
80g/m^2 PI-PMOEs fiber paper/Si-MWCNTs/PR (50PI-PMOEs/Si-MWCNTs/PR)	60	40

2.4 Characterization

The chemical structures of the synthesized PMOE and MWCNT before and after silanization were analyzed by Fourier transform infrared spectroscopy (FTIR, Nicolet is10, Thermo Fisher Scientific, USA) with a resolution of 4 cm^{-1} and sixteen scans. It is noted that MWCNT specimens were powdered using an agate mortar under a drying lamp. The surface elemental composition and the functional groups of various fibers were detected by X-ray photoelectron spectroscopy (XPS, Thermo ESCALAB 250XI, Thermo Fisher Scientific, USA) with a monochromatic Al K source (1486.6 eV). A curve fitting program (XPS Peak Fit software) was used to fit the XPS peaks with one or more Gaussian-Lorentz functions. The various fibers, fractured surfaces of the composites, carbonaceous residue on different surfaces after flame combustion and high-temperature treatment of the composites were characterized using scanning electron microscopy (SEM, SU151, Hitachi, Japan). Before imaging, the specimens were coated with gold-platinum to make the specimen conductive to prevent the accumulation of static electric charge during scanning electron microscopy. The thermal stabilities of various fibers and composites were determined by using a thermogravimetric analyzer (TG 209F1, Netzsch, Germany) from 400 to 800°C and 900°C, respectively, with a heating rate of 10°C/min in a nitrogen environment. The particle size of MWCNTs before and after silanization in an ethanol dispersion was estimated by a particle size analyzer (CC-100, Brookhaven, USA). The two dispersions were diluted to 0.01 mg/mL with ethanol before measurement. At least 5 values of particle size for each dispersion were tested, and the average result was taken. The X-ray diffraction (XRD, D2 Phaser, Bruker, USA) patterns of the various fibers were recorded using a PANalytical X'Pert PRO diffractometer. The Cu Kα ($\lambda = 0.154$ nm) radiation source was operated at 45 kV and 40 mA with a scan range (2θ) between 5° and 90°. A curve fitting program (Jade software) was used to fit the XRD patterns, and the relative crystallinity (X_c) was calculated via the following equation:

$$X_c = \frac{\sum I_c}{\sum I_c + \sum I_a} \times 100\% \tag{1}$$

where $\sum I_c$ is the diffraction integral intensity of the crystalline region and $\sum I_a$ is the scattering integral intensity of the amorphous region.

The three-dimensional morphology of the fiber surface was analyzed by atomic force microscopy (AFM, Dimension ICON, Bruker, Germany) performed on a multimode instrument in tapping mode using a monolithic Si tip with a resonance frequency between 250 and 300 kHz. In addition, the fiber surface roughness, including root mean square roughness (R_q) and arithmetic average roughness (R_a), was calculated by the following equations:

$$R_q = \sqrt{\frac{1}{N^2} \sum_{i=1}^{N} \sum_{j=1}^{N} \left(z_{ij} - z_{av}\right)^2} \tag{2}$$

$$R_a = \frac{1}{N} \sum_{i=1}^{N} \sum_{j=1}^{N} \left|z_{ij} - zcp\right| \tag{3}$$

where N is the number of pixels in the image; i and j are the pixel locations on the AFM image, respectively; z_{ij} is the peak height at locations i and j; z_{av} is the average height within the given area; and z_{cp} is the height from the center plane.

The contact angles of various fibers were evaluated with a dynamic contact angle tensiometer (DCAT-21, Dataphysics, Germany). After the values of the contact angle to the experimental liquids were determined, the surface free energy (γ_f) of the fiber was calculated in terms of Owens and Wendt's method using the following equations [38, 39]:

$$\gamma_l(1 + \cos\theta) = 2\sqrt{\gamma_l^d \gamma_f^d} + 2\sqrt{\gamma_l^p \gamma_f^p} \qquad (4)$$

$$\gamma_f = \gamma_f^d + \gamma_f^p \qquad (5)$$

where θ (°) is the contact angle at the fiber/liquid interface; γ^d (mJ/m^2) and γ^p (mJ/m^2) represent the dispersive and polar components of the surface free energy, respectively; the subscript l indicates the test liquid; and the subscript f indicates the various fibers.

The fiber dispersion degree was used to evaluate the dispersion stability of the fiber suspension. The fiber/deionized water suspension at a concentration of 3 wt.‰ was well prepared. The settlement state of the suspension after standing for 24 h was recorded, and the dispersion degree (f) of the fibers was calculated using the following equation:

$$f = \frac{v_0 - v_1}{v_0} \times 100\% \qquad (6)$$

where v_0 (mL) is the total volume of the suspension initially and v_1 (mL) is the volume of the supernatant in the suspension after standing for 24 h.

A specimen (3 × 3 cm^2) was cut from the fiber paper, and the pore size distribution of the fiber paper was analyzed by a porous-material pore-size analyzer (CFP-1100A; PMI, USA). The tensile tests of composites were conducted on a universal tensile testing machine (UTM6502, Sans, China) at a tensile rate of 2 mm/min according to the standard ASTM D638, and the specimens were dumbbell-shaped with sizes of 75 mm × 10 mm × 2 mm. Five parallel specimens for each composite were employed in the tensile tests. The limiting oxygen index (LOI) values of the composites with splines of 130 mm × 6.5 mm × 3.2 mm were determined using an oxygen index analyzer (OI-3, Deatak, USA) according to ASTM D2863. According to ASTM D3801, a vertical combustion tester (CZF-2, Jiangning Analytical Instrument Co., Ltd., China) was used to measure the UL-94 values of the composites, and the specimen dimensions were 120 mm × 13 mm × 3.2 mm. The heat release rate of the composites was evaluated using a microscale combustion calorimeter (MCC-2, GOVMARK, USA) based on ASTM D7309-07. The specimens were approximately 4 mg and were heated at a constant heating rate of 1℃/s from room temperature to 800°C under nitrogen at 80 cm^3/min. Then, the volatile, anaerobic thermal degradation products in the nitrogen gas stream were mixed with a 20 cm^3/min stream of 20% oxygen and 80% nitrogen prior to entering the combustion furnace at 900°C. Two composite specimens of 2 × 2 cm^2 were exposed to an ethanol flame for 120 s, and the combustion process was recorded by a digital camera. The electrical conductivity of the specimens was measured using a semiconductor parameter analyzer (4155C, Agilent Technologies Inc., China). Five parallel specimens for each composite were employed in this test.

3 Results and Discussion

3.1 Surface Growth and Characterization of the PI Fiber

Horseradish peroxidase (HRP) is mainly produced by the horseradish plant and is a glycoprotein complex composed of a colourless enzyme protein and dark brown iron porphyrin. As a kind of green biological enzyme, HRP is widely used in chemical catalysis as a result of its good stability and the catalytic modification of aromatic compounds in the presence of H_2O_2 [40–42]. The growth mechanisms of the irregular PMOEs network on the PI fiber surface under HRP catalysis are as follows: i) Chain initiation: Sodium percarbonate (SPC), which is called "solid hydrogen peroxide", is an adduct of H_2O_2 and sodium carbonate and can release H_2O_2 in the solvent [43]. HRP acts as a catalyst to catalyse the oxidation of PI fibers in the presence of H_2O_2. Therefore, HRP was oxidized by H_2O_2 to highly active HRP I. HRP I captured a hydrogen atom at the meta position of the amide group of the benzene ring to generate a free electron (represented by PI·). ii) Chain propagation: PI· captured a hydrogen atom on the C = C group at the end of the PMOE chain to generate the PMOE radical (represented by PMOE·), resulting in homopolymerization of PMOE on the PI fiber surface. iii) Polymerization of the monomer PMOE and PI· led the PMOE branched chain to be grafted onto the PI fiber main chain. Ultimately, the long chains of phosphate monoester (PMOEs) network grew on the PI fiber surface by crosslinking and entanglement of multiple branched chains [44, 45] Scheme 2.

The surface micromorphologies of various fibers are shown in Fig. 1a-d. The pristine PI fiber presented a smooth and neat surface, which greatly reduced the interface performance of the fiber (Fig. 1a). In contrast, all kinds of PI-PMOEs fibers showed surface morphologies with different roughness values. It was found that the lower concentration of the monomer resulted in a smaller molecular weight of the resulting polymer, which could only form intermittent "fish-scale" structures on the fiber surface (Fig. 1b). With increasing monomer addition, free radical reactions occurred at more sites on the fiber surface, leading to more intense polymerization and increased molecular weight of PMOE. The molecular chain was extended, and "petal" aggregates were grown to the outside of the fiber surface (Fig. 1c). The appearance of "filament" structures was attributed to the physical entanglement and chemical crosslinking between long chains of the polymer. Most of the long PMOEs chains were closely connected on the fiber surface to form a dense network, which increased the coating density of the polymer. The remaining chains extended out of the fiber surface (Fig. 1d).

To further confirm that the PMOEs network grew on the fiber surface, the three-dimensional morphology (Fig. 1e-h) and surface roughness (Fig. 1i) of the fibers were analyzed by AFM. The pristine PI fiber surface was smooth (Fig. 1e). With increasing PMOE concentration, the surfaces of all kinds of PI-PMOEs fibers became rougher, and many bumps appeared. Moreover, the fiber surface roughness was evaluated by the arithmetic average roughness (R_a), root mean square roughness (R_q) and average maximum height difference (R_{tm}). It is worth noting that the surface roughness of the fiber was greatly improved only with less monomer addition (Fig. 2f). The values of R_a and R_q increased from 36 nm and 53 nm to 180 nm and 223 nm, respectively. The aggregation of entangled long chains on the fiber surface increased the R_{tm} by 197 nm. Up to a PMOE dose of 20 mL (Fig. 1h), the R_a and R_q values increased to 326 nm and 411 nm, respectively, and R_{tm} also reached 634 nm. Higher R_{tm} values indicate that there are more PMOEs networks on the fiber surface. The extended polymer molecular chains provided more contact sites
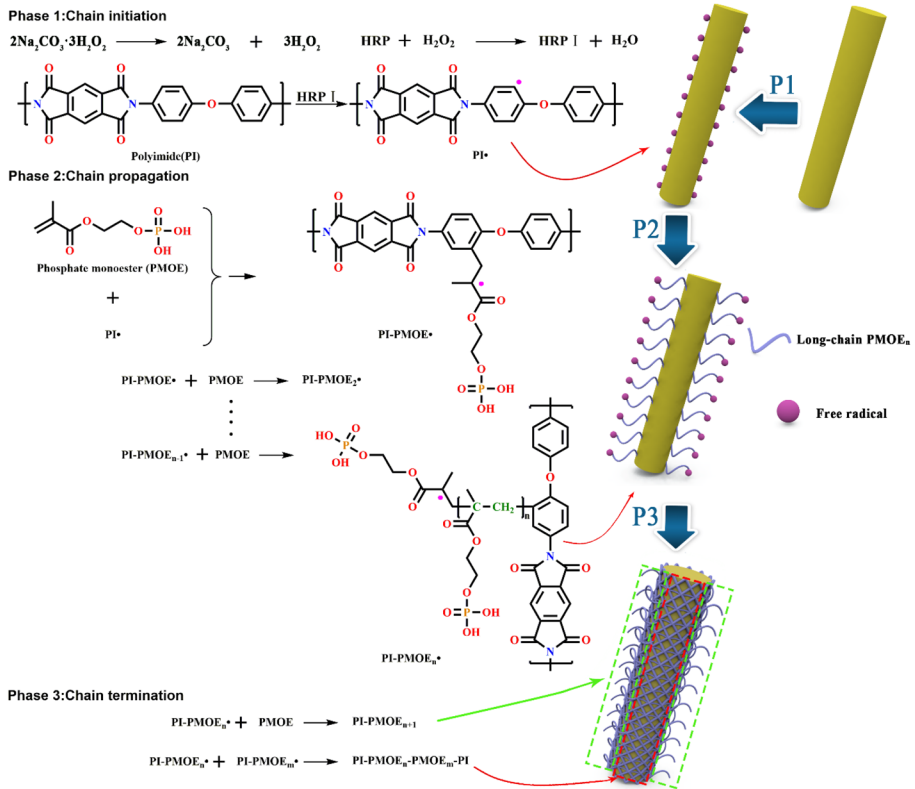
Scheme 2. Schematic illustration of PMOE growth on the surface of polyimide (PI) fiber initiated by enzyme (HRP) catalyst.

for the interface between the fiber and matrix, which is helpful to improve the mechanical interlock. In addition, the observed micromorphologies proved that the network density and average height of PMOEs can be adjusted by the PMOE concentration during the preparation process.

The changes in the polymer crystal structure of the fibers can be analyzed by the X-ray diffraction technique. Figure 1j displays the XRD patterns of pristine PI fibers and all kinds of PI-PMOEs fibers, and the relative crystallinity (X_c) is shown in Fig. 1k [46, 47]. There are many amorphous regions in the pristine PI fiber structure, indicating that the fiber is a semicrystalline polymer with a certain intensity diffraction peak and an X_c of 18.63%. After HRP catalytic treatment, the diffraction peak intensity of the fiber was weakened, and the crystallinity was slightly decreased. This is mainly due to the fact that PBS in the reaction mixture was alkalescent, while PI fibers have poor alkali resistance. It is difficult to remove the small molecules by Soxhlet extraction because they penetrated into the fiber after the surface structure of the fiber changed. Therefore, the stereoregular structure of the fiber polymer chain was slightly damaged, and the tight packing between the macromolecular chains was weakened, which further reduced the crystallization performance.

The specific contents of chemical elements and functional groups on the surface of the fiber can be analyzed by XPS [48]. Figure 2 shows the XPS spectra of pristine PI fiber
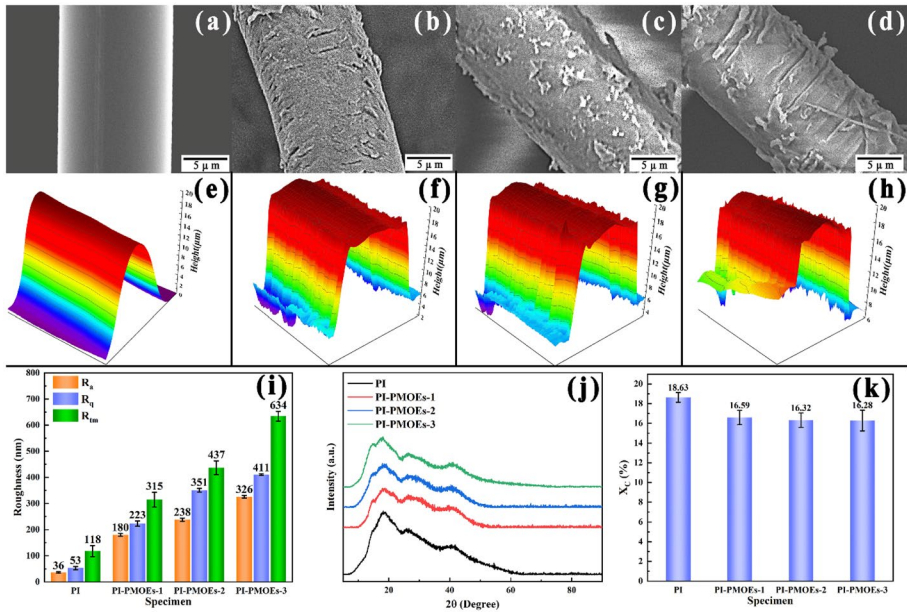
Fig. 1. SEM micrographs and AFM micrographs of (**a** and **e**) pristine PI fiber, (**b** and **f**) PI-PMOEs-1 fiber, (**c** and **g**) PI-PMOEs-2 fiber and (**d** and **h**) PI-PMOEs-3 fiber; (**i**) results of roughness of various fibers; (**j**) XRD patterns of various fibers; (**k**) The relative crystallinity of various fibers

and various PI-PMOEs fibers. Each element (C, O, and P) peak was fitted into multiple constituent peaks to determine the relative contents of different functional groups. Three markedly intense peaks (O1s, N1s, and C1s) were displayed in the spectrum of pristine PI fiber. It is noted that the new P2p and P2s peaks contained in the spectra of all kinds of PI-PMOEs fibers, and we chose the P2p peak as the quantitative analysis standard for P. The PMOEs on the surface of various PI-PMOEs fibers contain a large number of oxygen-containing groups (O-C, O = C, O = P, and O-P), leading to an increase in the intensity of the O1s peak. The PMOEs network growing on the fiber surface limited the detection of N only in the fiber structures since the detection depth of XPS technology is approximately 10 nm, which explained the weakening of the N1s peak intensity. The intensity of the element peak is determined by the proportion of the element, so an increase in the other elemental peak intensities led to a decrease in the C1s peak intensity.

Furthermore, the C1s spectrum of the pristine PI fiber exhibited four obvious peaks (Fig. 2b), which are located at 284.7 eV (C-C/C-H), 285.8 eV (C-N), 286.4 eV (C-O), and 288.2 eV (N-C = O). An additional peak in the C1s spectrum (Fig. 2e, h, and k) was observed at 288.6 eV (O-C = O). Simultaneously, the contents of the C-O and O-C = O groups increased gradually with increasing PMOE concentration and increased to 29.9% and 7.4%, respectively (Fig. 2m). Moreover, the O1s spectrum of pristine the PI fiber (Fig. 2c) exhibited two peaks at 531.9 eV (O-C) and 533.5 eV (O = C). The O1s spectrum of the PI-PMOEs-1 fiber (Fig. 2f) showed two additional peaks at 532.3 eV (O = P) and 532.8 eV (O-P). The contents of O = P and O-P groups in the PI-PMOEs-3 fiber also reached 10.8% and 19.1%, respectively (Fig. 2n), indicating that the PMOEs network successfully grew on the fiber surface. The P2p splitting peaks at 133.8 eV ($2p_{1/2}$) and 134.7
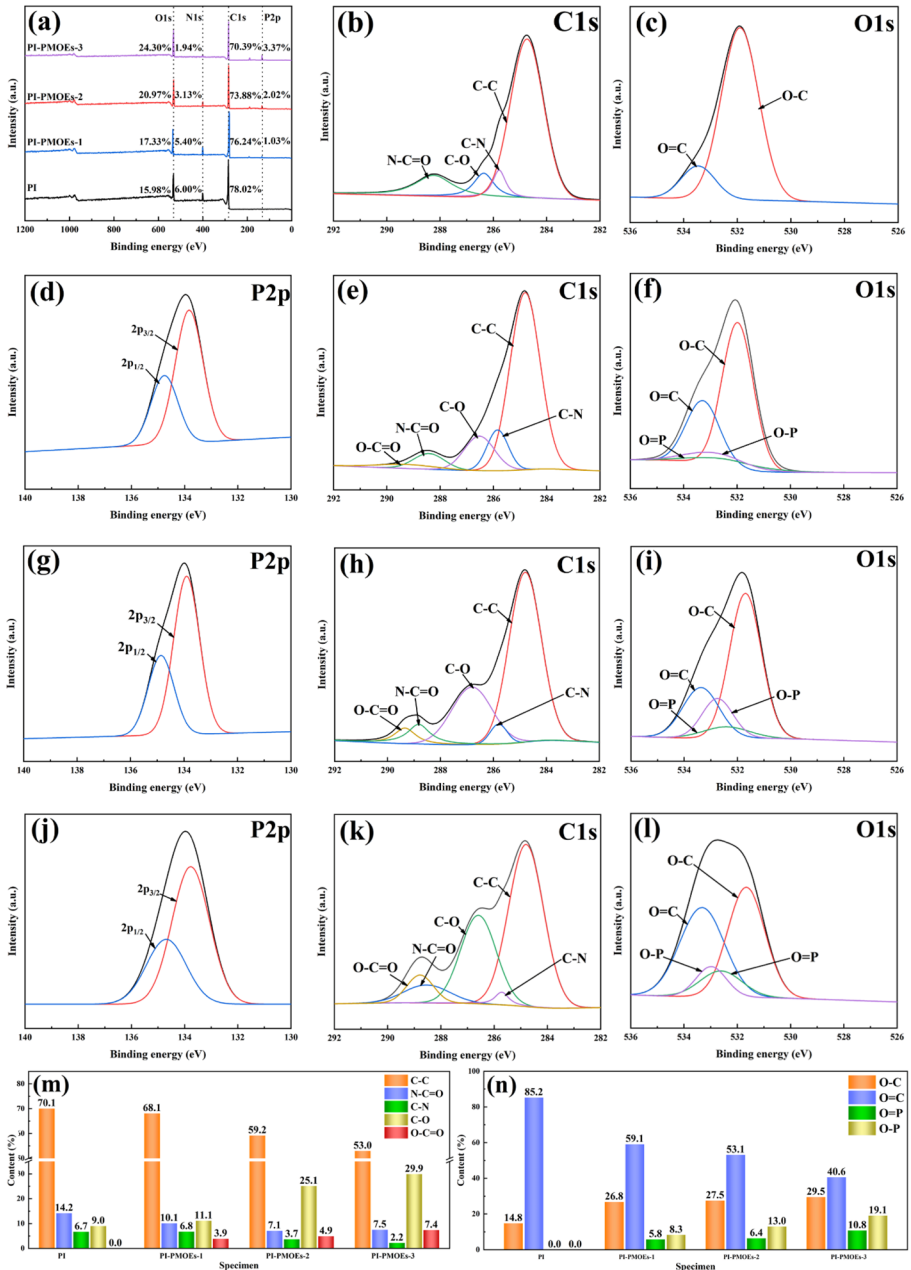
Fig. 2. (**a**) Wide scan XPS spectra and calculated elemental concentrations of various fibers; (**b**) C1s and (**c**) O1s XPS spectra of pristine PI fiber; (**d**) P2p, (**e**) C1s and (**f**) O1s XPS spectra of PI-PMOEs-1 fiber; (**g**) P2p, (**h**) C1s and (**i**) O1s XPS spectra of PI-PMOEs-2 fiber; (**j**) P2p, (**k**) C1s and (**l**) O1s XPS spectra of PI-PMOEs-3 fiber; (**m**) C1s and (**n**) O1s curve fitting results of various fibers

eV ($2p_{3/2}$) were found in the P2p peak spectra of the three kinds of PI-PMOEs fibers, which further confirmed the existence of PMOEs [49, 50].

Thermogravimetric analysis (TGA) under a N_2 atmosphere was used to evaluate the thermal stability of the fibers [51]. The TGA and DTG curves of various fibers are shown in Fig. 3a-b, and the typical thermodegradation data, including the initial degradation temperature (T_{di}), the maximum degradation rate temperature (T_{max}) and the char yield ratio (Y_c), are summarized in Table 2. The pristine PI fiber showed a maximum degradation
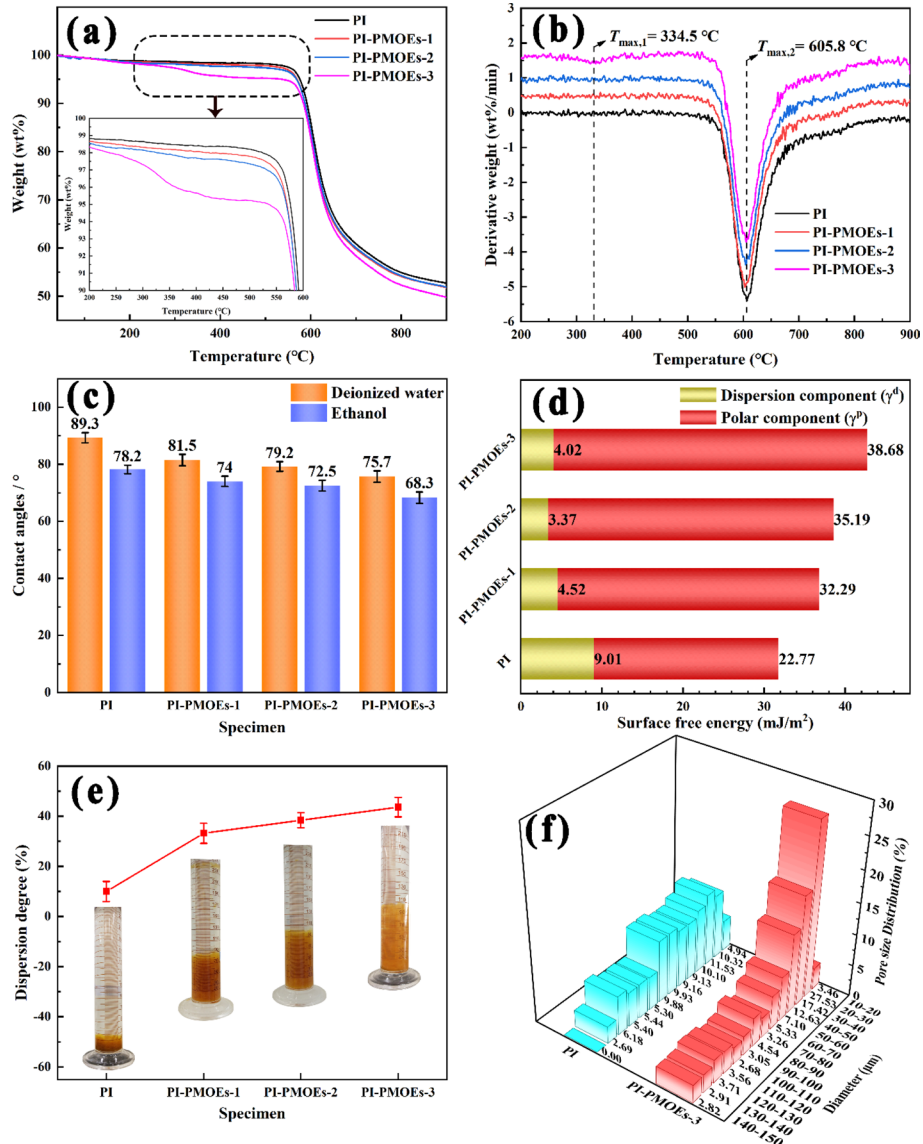

Fig. 3 (**a**) TGA and (**b**) DTG thermograms of various fibers under N_2 atmosphere; (**c**) contact angles and (**d**) surface free energy of various fibers; (**e**) dispersion degree and dispersion state of fibers in water; (**f**) Pore size distribution of fiber paper

Table 2. Typical thermodegradation data of various fibers under N_2 atmosphere

Specimen	Phase 1			Phase 2		
	$T_{di,1}$ (℃)	$T_{max,1}$ (℃)	$Y_{c,1}$ at 500℃ (wt.%)	$T_{di,2}$ (℃)	$T_{max,2}$ (℃)	$Y_{c,2}$ at 900℃ (wt.%)
PI	-	-	-	490.1	605.8	52.70
PI-PMOEs-1	-	-	-	472.5	603.2	51.81
PI-PMOEs-2	-	-	-	475.1	604.6	51.92
PI-PMOEs-3	279.6	334.5	97.81	480.3	605.2	49.80

rate at 605.8℃ and one mass loss stage at 490.1-800.2℃, which indicated that the PI fiber exhibited excellent thermal stability. Comparatively, another weight loss of approximately 2.19 wt.% was observed at 279.6℃-503.5℃ only in the TGA thermogram of the PI-PMOEs-3 fiber, which is likely attributed to the thermal decomposition of the PMOEs network growing on the fiber surface. This phenomenon is due to the small molecular weight of the polymers on the surface of PI-PMOEs-1 and PI-PMOEs-2 fibers, and a more complete PMOEs network was not formed. As mentioned above, the molecular chain regularity of the fiber was destroyed after the HRP catalytic treatment. Therefore, the high-temperature resistance of the fibers was affected to some extent, and the Y_c value at 900℃ of all kinds of PI-PMOEs fibers was slightly decreased.

The purpose of this study is to improve the dispersibility of PI fibers in the medium, and the increase in surface free energy is conducive to promoting the interfacial properties and hydrophilicity of the fiber. Therefore, the contact angles between the experimental liquids and the surface free energy were measured and calculated in Fig. 3c-d to evaluate the wettability of the various fibers. It was observed that the contact angles of the pristine PI fiber with strongly polar deionized water and weakly polar ethanol were 89.3º and 78.2º, respectively. In contrast, the contact angles of all kinds of PI-PMOEs fibers with two kinds of wetting liquids decreased significantly. The surface free energy (γ_f) of PI-PMOEs-3 fiber was 42.70 mJ/m^2, which was an increase of 34.36% compared to that of the PI fiber. The increase in various PI-PMOEs fiber surface free energies was attributed to the fiber's higher surface roughness and larger specific surface area, so the fiber was more likely to overcome the surface tension of the liquids and the liquids were easier to spread on the fiber surface. It is interesting to note that the increase in surface free energy of various PI-PMOEs fibers was mainly due to the contribution of the polar component (γ^p), which resulted in enhancement of the surface polarity, inductive effect and the influence of hydrogen bonds. Furthermore, an increase in the number and types of polar functional groups led to higher affinity of three kinds of PI-PMOEs fibers with deionized water than of ethanol. Therefore, it was found that the contact angle of PI-PMOEs-3 fiber with deionized water decreased by 13.6°, while that with ethanol decreased by only 9.9°.

To evaluate the dispersion stability of various fibers more intuitively, the dispersion degree of a fiber suspension and the pore size distribution of fiber paper were measured and are shown in Fig. 3e-f. The dispersion degree of pristine PI fibers was 10.0%, while the dispersion degree of all kinds of PI-PMOEs fibers increased. The dispersion degree of the PI-PMOEs-3 fibers reached 43.6%, a relative increase of 33.6%. The pore size of the pristine PI fiber paper prepared by vacuum-assisted wet papermaking technology varied. By comparison, the pore size of the PI-PMOEs-3 fiber paper was smaller, and the pore size distribution

was relatively uniform. The proportion of pores with a diameter of 20-50 μm was 57.58%, and that of pores with a diameter of 20-30 μm was 27.53%. This phenomenon is attributed to the high inertness of the pristine PI fiber surface, which will form compact "cotton ball" or "flocculent" fiber clusters under van der Waals forces. Once this structure formed, the fibers became more hydrophobic and hindered the dispersion of other fibers. The poor dispersion stability of the fiber suspension also resulted in more fiber bundles and an uneven number of fiber layers in the fiber paper. However, there were more polar groups on the rough surface of the PI-PMOEs-3 fiber, which led to a higher affinity of the fiber for the aqueous media and stronger repulsion between the fibers. The fiber bundles were more easily dispersed into single fibers and formed a large three-dimensional network with a uniform pore size in the process of vacuum-assisted wet papermaking. In conclusion, the hydrophilicity of PI-PMOEs fibers improved with increasing PMOE concentration, which is beneficial for enhancing the interfacial properties of the fibers. Moreover, the paper formation of PI-PMOEs-3 fibers fabricated by vacuum-assisted wet papermaking technology also improved.

3.2 Mechanical Properties of PI-PMOEs Fiber-Reinforced Si-MWCNTs/PR Composites

The mechanical properties of Si-MWCNTs/PR composites containing different amounts of PI fibers and PI-PMOEs fibers were evaluated. Figure 4a-b shows the resulting tensile strength and elongation at break of each of the composites. Obviously, Si-MWCNTs/PR composites with better tensile properties can be obtained by introducing longer flexible PI fibers compared with those of PR composites with only Si-MWCNTs as reinforcement fillers. It was found that the tensile strength improved linearly with increasing fiber content from 20.29 MPa (Si-MWCNTs/PR) to 75.02 MPa (80PI/Si-MWCNTs/PR). This is due to the fact that PI fibers with high strength and a high modulus improved the energy consumption of the 80PI/Si-MWCNTs/PR composites during break, resulting in enhanced mechanical properties of the composites [52]. It is worth noting that the tensile strength of the composite with PI-PMOEs fibers as a reinforcing filler further increased by 21.59% to 91.22 MPa (80PI-PMOEs/Si-MWCNTs/PR). This phenomenon is most likely due to the anchoring of the PMOEs network and Si-MWCNTs network constructed at the interface between the PI-PMOEs fibers and the matrix. The interface adhesion was enhanced, and the stress transmission efficiency was improved. On the other hand, the pore size distribution of PI-PMOEs fiber paper was more uniform (Fig. 3f), and the contact area between the matrix and PI-PMOEs fibers increased. The combination of the two phases was stronger, which is beneficial to the transfer of stress from the matrix to the fiber via the shear transfer mechanism [53]. In addition, it was found that the elongation at break of the composites showed an increasing trend similar to that of the tensile strength. This results from the fact that the failure mode of the composites gradually transitioned from brittle breakage to ductile fracture, and the ductility of the composites was improved. Compared with the straight and smooth PI fiber surface, PI-PMOEs fibers with higher roughness can interact with the matrix to retard fiber pullout and promote fiber rupture, so the elongation at break was further improved.

After that, the fracture mechanism of the fiber-reinforced Si-MWCNTs/PR composites was qualitatively analyzed by observing the micromorphologies of the fracture surfaces in Fig. 4c-h. It can be seen from Fig. 4c-e that the PI fibers drawn from the composite have smooth and neat surfaces, and the debonding and pullout of the
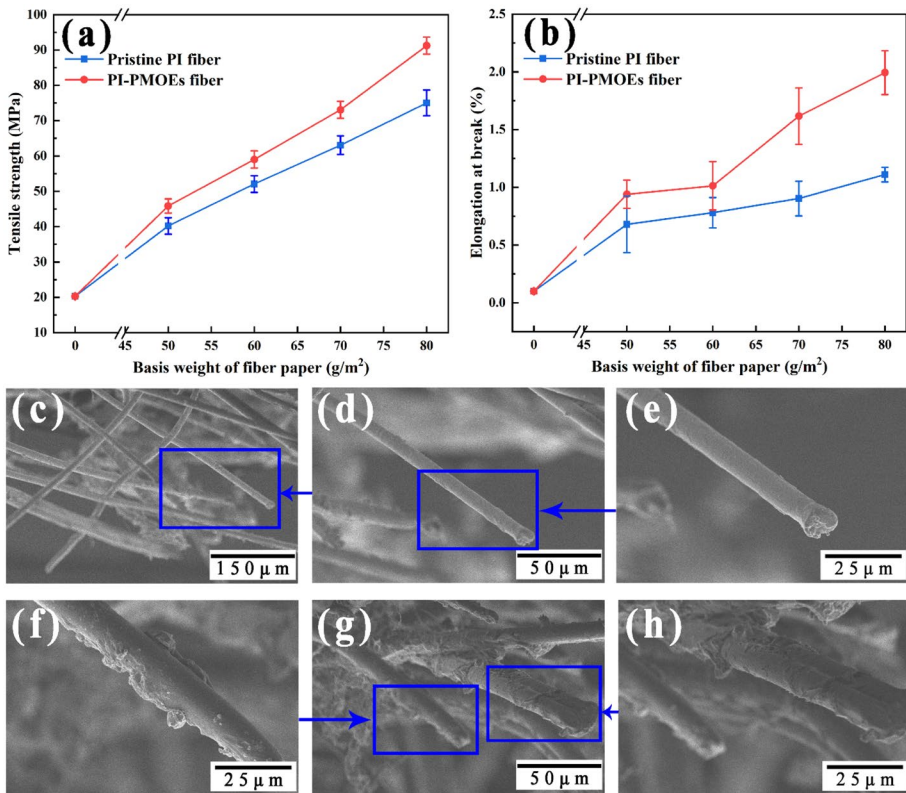
Fig. 4. Tensile properties of Si-MWCNTs/PR and its composites: (**a**) tensile strength, (**b**) elongation at break; SEM micrographs of fracture surfaces: (**c-e**) 80PI/Si-MWCNTs/PR composite, (**f-h**) 80PI-PMOEs/Si-MWCNTs/PR composite

fibers were the main means of energy consumption during fracture. The propagation of cracks during fracture of the sample was hindered, which increased the tensile strength of the composite. However, it is undeniable that the interface between the matrix and the fibers was still poor, and the mechanical properties of the composite were less than expected. It is obvious that the fracture surface of the 80PI-PMOEs/Si-MWCNTs/PR composite showed a highly rough PI-PMOEs fiber surface, and the pulled fiber surface adhered to a large amount of matrix (Fig. 4f-h). The improvement of fiber surface activity enhanced the interfacial adhesion. On the other hand, the two networks interpenetrate at the resin-fiber interface, which further increases the interfacial bonding strength. In the end, a stronger mechanical interlock formed between the PI-PMOEs fibers and the resin matrix. Furthermore, the uniformly dispersed Si-MWCNTs in the matrix bore part of the external load, and the load transferred to the fiber was reduced, which plays a toughening role in the composite [54]. In general, the relatively concentrated stress in the composite was released, and the resistance of crack generation and propagation was increased, so the mechanical properties were further improved.

3.3 Thermal Stability and Flame Retardancy of PI-PMOEs Fiber-Reinforced Si-MWCNTs/PR Composites

Thermal degradation is primarily important for assessing the fire resistance of composites. The TGA and DTG curves of Si-MWCNTs/PR and all 80PI-PMOEs/Si-MWCNTs/PR composites are shown in Fig. 5a, b and summarized in Table 3. It was found that the thermal degradation of the Si-MWCNTs/PR composite exhibited three weight loss stages. The first weight loss, observed in the range of 100-220℃, was due to the residual moisture after PR curing and small molecules such as formaldehyde volatilized by the PR after further condensation. The weight loss at 360-550℃ corresponded to the main stage of the thermal degradation of PR. The process is that PR further crosslinks and cyclizes to form carbides and releases hydrocarbon and alcohol pyrolysis products such as methane [55]. The final stage of pyrolysis observed at 570-660℃ was attributed to PR dehydrogenation and carbonization. At the same time, a certain amount of small molecules, such as CO, CO_2, and CH_4, were released. The data in Table 3 also show that the residual char mass of the Si-MWCNTs/PR composite was the lowest at 600℃ and 800℃. In contrast, when PI-PMOEs fibers were introduced into the Si-MWCNTs/PR composite, the composites showed a greater increase in the residue after thermal degradation. The increase in the residual amount results in further enhancement of the thermal stability of the composite. Interestingly, the PI-PMOEs/Si-MWCNTs/PR composites exhibited five stages of thermal
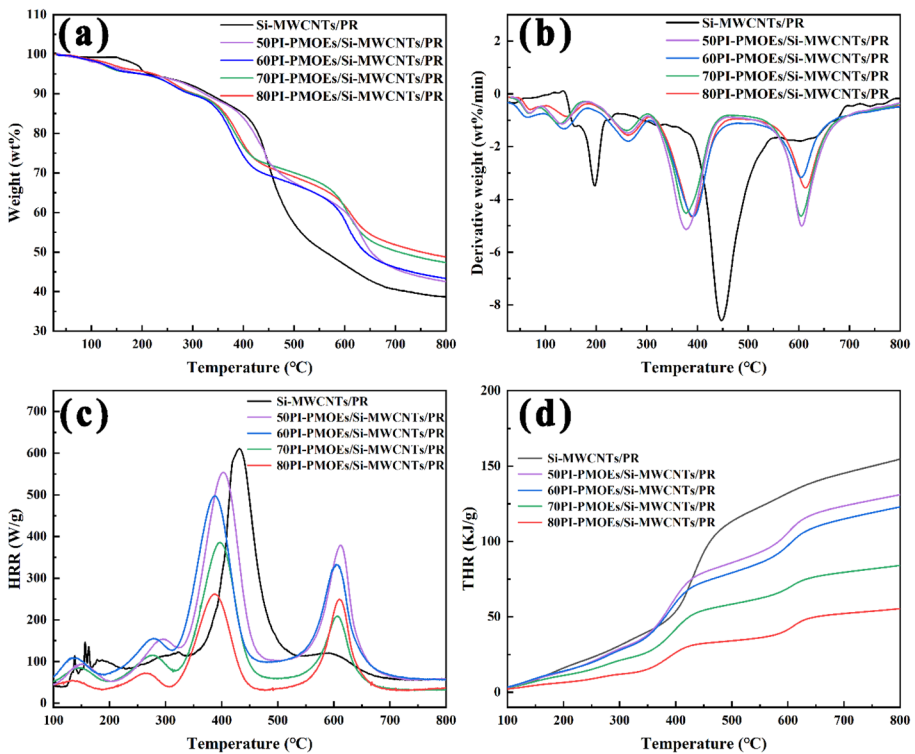

Fig. 5. (**a**) TGA and (**b**) DTG thermograms of Si-MWCNTs/PR and its composites under N_2 atmosphere; (**c**) heat release rate and (**d**) total heat release curves of Si-MWCNTs/PR and its composites

Table 3. Typical thermodegradation data of Si-MWCNTs/PR and its composites under N_2 atmosphere

Specimen	$T_{10wt.\%}$ [a] (℃)	Y_c at 600℃ (wt.%)	Y_c at 800℃ (wt.%)
Si-MWCNTs/PR	329.9	46.7	38.6
50PI-PMOEs/Si-MWCNTs/PR	322.5	60.3	42.5
60PI-PMOEs/Si-MWCNTs/PR	291.5	57.8	43.8
70PI-PMOEs/Si-MWCNTs/PR	298.2	61.3	47.4
80PI-PMOEs/Si-MWCNTs/PR	302.6	61.7	48.8

a $T_{10wt.}\%$ is defined as the temperature of 10 wt.% weight loss in the TGA curve.

decomposition. The moisture evaporation and thermal decomposition of the volatilization of small molecules were advanced to 40-90℃ and 90-180℃, respectively. This may have resulted from the large three-dimensional interconnected structure formed between PI-PMOEs fibers, which provided bridges for Si-MWCNTs, while the Si-MWCNTs with high thermal conductivity accelerated heat transfer and promoted thermal decomposition of composites. However, the thermal conductivity of the PI-PMOEs fiber itself is poor, and it cannot provide enough heat to support the next stage of thermal decomposition in time. Therefore, the decomposition temperature range of the remaining small molecule groups in PR was delayed to 200-300℃, and the maximum decomposition rate was relatively low. This stage was followed by further heat transfer within the composite, and the main crosslinking and carbonization stages of PR thermal degradation also occurred at 300-450℃. This is due to PI-PMOEs fibers have good high-temperature resistance and form a strong network of "large skeleton" after uniform dispersion, and the Si-MWCNTs and carbonized PR matrix also formed "small skeleton" network connection. The two networks overlap to establish an effective physical barrier layer, which greatly reduces the maximum thermal degradation rate. The last temperature range of 500-700℃ was attributed to the thermal decomposition of PI-PMOEs fibers, which also corresponded to the results of the thermal decomposition of fibers in Fig. 4a. In general, using PI-PMOEs fibers as the reinforcing fillers of Si-MWCNTs/PR composites helps to improve the thermal stability and enhance the flame retardancy.

Microcombustion calorimetry (MCC) is a new, convenient and fast detection method. As a small-scale flammability test technology, MCC requires only a few milligrams of sample to measure the heat release when chemicals are decomposed during the combustion process and to eliminate physical factors such as swelling, dropping and shielding unrelated to the test results [56]. The peak heat release rate (PHRR) and the total heat release rate (THR) reflect the potential combustion characteristics of the composite and evaluate its fire resistance. A lower value indicates that the composite is less flammable. As shown in Fig. 5c-d, the PHRR of the Si-MWCNTs/PR composite reached 611.3 W/g at 360-550℃, and the THR was as high as 154.6 KJ/g. This result indicated that the composite released a large amount of heat during the combustion process and had high flammability. With the increase in PI-PMOEs fiber content in the composites, the PHRR at 300-450℃ decreased gradually to 262.3 W/g. The increase in PHHR at 500-700°C was due to the thermal decomposition of PI-PMOEs fibers. In addition, the THR of PI-PMOEs/Si-MWCNTs/PR composites also showed a similar downward trend as that of PHRR, with a maximum decrease to 55.7 KJ/g and a relative decrease of 64.0%. This further illustrated that a stable char layer supported by fibers was formed after carbonization of the composite,

Table 4. LOI and UL-94 data of Si-MWCNTs/PR and its composites

Specimen	LOI (vol%)	UL-94	
		Rating	Dropping
Si-MWCNTs/PR	23.0	N.R.	dropping
50PI-PMOEs/Si-MWCNTs/PR	29.8	V-1	no dropping
60PI-PMOEs/Si-MWCNTs/PR	32.1	V-1	no dropping
70PI-PMOEs/Si-MWCNTs/PR	33.4	V-1	no dropping
80PI-PMOEs/Si-MWCNTs/PR	35.0	V-0	no dropping

which hindered the further transfer of heat and mass. The above results are consistent with the TGA results of the composites, which proved that PI-PMOEs fiber-reinforced Si-MWCNTs/PR composites have potential fireproof application value.

The combustibility of Si-MWCNTs/PR and PI-PMOEs/Si-MWCNTs/PR composites was investigated by LOI and UL-94 testing, as listed in Table 4. It was observed that the LOI value of the Si-MWCNTs/PR composite was only 23.0%. The composite failed the UL-94 test, combustion decreased, and self-extinguishing occurred during dropping. When the mass ratio of PI-PMOEs fiber paper was 25 wt.%, the LOI value of the composite reached 29.8% and passed the UL-94 V-1 level rating. Upon increasing the amount of PI-PMOEs fibers, the LOI values of the 60PI-PMOEs/Si-MWCNTs/PR, 70PI-PMOEs/Si-MWCNTs/PR and 80PI-PMOEs/Si-MWCNTs/PR composites increased to 32.1%, 33.4%, and 35.0%, respectively, and the 80PI-PMOEs/Si-MWCNTs/PR composite passed the UL-94 V-0 rating.

To analyze the fire resistance of fiber-reinforced composites more intuitively, Si-MWCNTs/PR and 80PI-PMOEs/Si-MWCNTs/PR composites were exposed to a 500-700℃ ethanol flame and a 500℃ high-temperature environment, and the relevant combustion process and sample appearance changes are shown in Fig. 6a-b for evaluation. As shown in Movie S1 in the Supporting Information, the Si-MWCNTs/PR and 80PI-PMOEs/Si-MWCNTs/PR composites were simultaneously moved into the ethanol flame, while they exhibited opposite flame-retardant behaviors. It can be seen that the Si-MWCNTs/PR composite was completely burned in approximately 30 s, during which black smoke escaped and dropped obviously. In comparison, the 80PI-PMOEs/Si-MWCNT/PR composite material exhibited better fire resistance, and there was no drop or black smoke during the combustion process. Even if the material was continuously exposed to high-temperature flame for 120 s, it was still inert to the flame. At the end of combustion, the composite maintained the contracted state of the original physical form without any change in shape. Moreover, after heat treatment at 500℃ for 10 min, the Si-MWCNTs/PR composite exhibited expansion and structural damage, while the 80PI-PMOEs/Si-MWCNTs/PR composite still showed good structural integrity without shrinkage. The above phenomena indicated that PI-PMOEs fibers as fillers effectively improved the resistance of Si-MWCNTs/PR composites to high temperature and flame.

The carbonaceous residual plays a crucial role in the flame retardant and smoke suppression performances, so increasing the char layer is an effective method to judge the improvement of flame retardancy of the composite. By studying the appearances and micromorphologies of the composites after combustion, the char residues can also be observed, and the flame-retardant mechanism can be analyzed. As mentioned above,
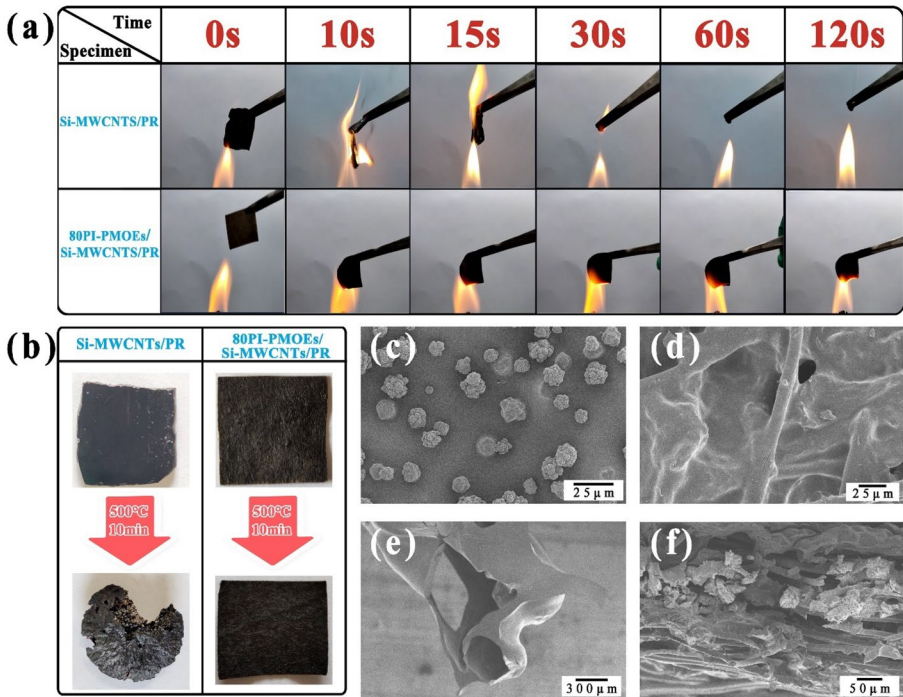
Fig. 6 (**a**) Combustion processes of Si-MWCNTs/PR and 80PI-PMOEs/Si-MWCNTs/PR composites; (**b**) digital images of Si-MWCNTs/PR and 80PI-PMOEs/Si-MWCNTs/PR composites before and after treatment at 500℃ for 10 min;(**c**) outer surface and (**e**) inner surface SEM micrographs of Si-MWCNTs/PR composite after treatment at 500°C for 10 min; (**d**) surface and (**f**) cross-sectional surface SEM micrographs of 80PI-PMOEs/Si-MWCNTs/PR composite after exposing it to the ethanol flame

Si-MWCNTs/PR composite has poor flame retardancy, and it is difficult to preserve a complete physical form after flame burning. Therefore, the micromorphologies of the composite surface after treatment at 500℃ for 10 min were observed and are shown in Fig. 6c and e. It is obvious that many globular particles with different sizes appeared on the outer surface char layer and were independent of each other. This is due to agglomeration of the resin-coated Si-MWCNTs upon carbonization and shrinkage of the matrix. However, this only occurred in a small region of the outer surface. As shown in Fig. 6b, the Si-MWCNTs/PR composite expanded, and a large number of holes appeared after high-temperature treatment. This phenomenon was attributed to the crosslinking and carbonization of the PR matrix and the release of gaseous molecules when the composite was exposed to the environment with a rapid temperature increase. Then, with the rapid increase in internal pressure, sufficient external thrust was generated, leading to the volume of the composite increasing sharply after heating. Many large-scale holes appeared in the composite concurrently (Fig. 6e), which also provided a channel for the release of combustible volatiles and the transfer of flame heat. In contrast, as shown in Fig. 6d and f, the surface of 80PI-PMOEs/Si-MWCNTs/PR exhibited a complete carbon layer and almost no pores after flame combustion. A tightly connected carbon layer appeared between the fiber layers, and the hole and crack size were relatively small. In general, the flame retardant mechanism of PI-PMOEs/Si-MWCNTs/PR composites

can be discussed in terms of three factors. The main reason for the observed results is that the "small skeleton" formed by the Si-MWCNTs and char layer after PR thermal degradation and the "large skeleton" formed by PI-PMOEs fibers jointly establish a continuous and dense network protective layer, which reduces the transportation efficiency of combustible gases such as oxygen. Second, the PI-PMOEs fibers have poor thermal conductivity and conjugated structures of aromatic heterocycles in the macromolecular chains. This provides high thermal oxygen stability for the fibers and inhibits the mass transfer from the matrix to the heat source. Finally, the noncombustible nitrogen-containing inert gas will be released during the thermal degradation of PI-PMOEs fibers, which dilutes the concentration of the combustible gas. The conditions that support combustion are destroyed, thereby preventing further thermal degradation inside the composite. The above results demonstrate that PI-PMOEs fibers have great potential as effective fire-retardant fillers for composites and can be used as a continuous layered structure to hinder the spread of flames.

3.4 Electrical Properties of PI-PMOEs Fiber-Reinforced Si-MWCNTs/PR Composites

We also measured the electrical conductivities of Si-MWCNTs/PR and PI-PMOEs/ Si-MWCNTs/PR composites, as listed in Table 5. Since Si-MWCNTs/PR composite is prepared in the mould, it has almost the same electrical conductivity in the plane and the thickness directions. It also shows good electrical conductivity. When PI-PMOES fiber is used as reinforcement filler, the electrical conductivity of the composite only decreases slightly in the plane direction. However, the electrical conductivity decreased a lot in the thickness direction. Even when the fiber paper reached 40 wt.% (the base weight of the paper was $80g/m^2$), the electrical conductivity decreased to 5.4×10^{-12} S/cm. The fibers in this article are composite with matrix in the form of paper. According to the seepage theory, when the fiber fillers are less, Si-MWCNTs nanoparticles can form a bridge and network along the thickness direction, and a complete conductive pathway can be formed. According to the percolation theory, we infer that Si-MWCNTs nanoparticles bridges and networks are formed along the thickness direction when the fiber filler is less [57–62]. Finally, a complete conductive pathway is formed. However, the filler reaches the percolation threshold with the increase of the proportion of fiber paper and the composite changes from the electrical conductor to insulator. In addition, PI-PMOES fiber and aramid fiber are the fillers with excellent insulation properties, which further reduce the conductivity of the composite in the thickness direction.

Table 5. The electrical conductivities of Si-MWCNTs/ PR and its composites

Specimen	In-plane (S/cm)	Through-the-thickness (S/cm)
Si-MWCNTs/PR	6.4×10^{-3}	6.2×10^{-3}
50PI-PMOEs/Si-MWCNTs/PR	4.7×10^{-4}	3.5×10^{-4}
60PI-PMOEs/Si-MWCNTs/PR	4.5×10^{-4}	2.4×10^{-5}
70PI-PMOEs/Si-MWCNTs/PR	3.2×10^{-4}	6.5×10^{-10}
80PI-PMOEs/Si-MWCNTs/PR	2.8×10^{-4}	5.4×10^{-12}

4 Conclusions

In conclusion, we have demonstrated a simple and effective strategy for preparing a novel PI-PMOEs fiber-reinforced Si-MWCNTs/PR composite with excellent mechanical and flame-retardant properties by using PI-PMOEs fibers catalysed by HRP as fillers. A new reinforcement method of polymer composite is introduced, in which the fiber is introduced into the composite material in the form of fiber paper. It was observed that PMOEs were closely connected to the surface of PI fiber. The PMOEs network on the fiber surface could be controlled by the concentration of the monomer. Furthermore, the surface roughness and active sites of the PI-PMOEs fiber increased. This improved the interfacial adhesion between the fiber and polymer matrix. Moreover, the pore size distribution of the fiber paper prepared by vacuum-assisted wet papermaking technology was uniform, which was attributed to the enhancement of the hydrophilicity of the fiber and was conducive to improving the stress transfer efficiency. Compared with that of the Si-MWCNTs/PR composite, the tensile strength of the 80PI-PMOEs/Si-MWCNTs/PR composite increased significantly by 267.9% when the fiber paper content was 40 wt.%. The composite also exhibited good flame retardancy, with a char residue rate of 48.8% and an LOI value of 35.0% at 800℃. It maintained the original physical shape after high-temperature burning of the ethanol flame. However, the electrical property of the composite became poor due to the percolation threshold and the insulating property of PI fiber. This work provides an eco-friendly and efficient method to improve the surface activity of PI fibers while maintaining their excellent original properties. It is expected that this work will provide a fundamental understanding of the remarkable action of the high-performance chemical synthetic fiber incorporated with carbon nanotube polymer composites on the substantial improvement of mechanical properties and flame retardancy.

5 Supporting Information

Electronic Supplementary Information (ESI) available: synthesis of phosphate monoester (PMOE) and silane functionalization of multiwalled carbon nanotubes (MWCNTs) in Section I and Section II, respectively. Additionally, the burning process of Si-MWCNTs/PR composite and 80PI-PMOEs/Si-MWCNTs/PR composite are shown in Movie S1.

Declarations

Conflict of Interest The authors declare no competing financial interest.

References

1. Park, S.H., Hwang, J., Park, G.S., Ha, J.H., Zhang, M., Kim, D., Yun, D.-J., Lee, S., Lee, S.H.: Modeling the electrical resistivity of polymer composites with segregated structures. Nat. Commun. **10**(1), 2537 (2019). https://doi.org/10.1038/s41467-019-10514-4

2. Kyrylyuk, A.V., Hermant, M.C., Schilling, T., Klumperman, B., Koning, C.E., van der Schoot, P.: Controlling electrical percolation in multicomponent carbon nanotube dispersions. Nat. Nanotechnol. **6**(6), 364–369 (2011). https://doi.org/10.1038/nnano.2011.40

3. Zheng, M., Chi, Y., Hu, Q., Tang, H., Jiang, X., Zhang, L., Zhang, S., Pang, H., Xu, Q.: Carbon nanotube-based materials for lithium–sulfur batteries. J. Mater. Chem. A. **7**(29), 17204–17241 (2019). https://doi.org/10.1039/C9TA05347F

4. Schneider, V., Polonskyi, O., Strunskus, T., Elbahri, M., Faupel, F.: Light-induced Conductance Switching in Photomechanically Active Carbon Nanotube-Polymer Composites. Sci Rep-Uk **7**(1), 9648 (2017). https://doi.org/10.1038/s41598-017-10211-6

5. Zeng, Y., Lu, G., Wang, H., Du, J., Ying, Z., Liu, C.: Positive temperature coefficient thermistors based on carbon nanotube/polymer composites. Sci Rep-Uk **4**, 6684 (2014). https://doi.org/10.1038/srep06684

6. Wu, Z., Wang, H., Tian, X., Ding, X., Xue, M., Zhou, H., Zheng, K.: Mechanical and flame-retardant properties of styrene–ethylene–butylene–styrene/carbon nanotube composites containing bisphenol A bis(diphenyl phosphate). Compos. Sci. Technol. **82**, 8–14 (2013). https://doi.org/10.1016/j.compscitech.2013.04.003

7. Zhan, G.-D., Kuntz, J.D., Wan, J., Mukherjee, A.K.: Single-wall carbon nanotubes as attractive toughening agents in alumina-based nanocomposites. Nat. Mater. **2**(1), 38–42 (2003). https://doi.org/10.1038/nmat793

8. Kashiwagi, T., Du, F., Douglas, J.F., Winey, K.I., Harris, R.H., Shields, J.R.: Nanoparticle networks reduce the flammability of polymer nanocomposites. Nat. Mater. **4**(12), 928–933 (2005). https://doi.org/10.1038/nmat1502

9. Zare, Y., Rhee, K.Y.: Simplification and development of McLachlan model for electrical conductivity of polymer carbon nanotubes nanocomposites assuming the networking of interphase regions. Composites, Part B **156**, 64–71 (2019a). https://doi.org/10.1016/j.compositesb.2018.08.056

10. Zare, Y., Rhee, K.Y.: Evaluation of the Tensile Strength in Carbon Nanotube-Reinforced Nanocomposites Using the Expanded Takayanagi Model. JOM. **71**(11), 3980–3988 (2019). https://doi.org/10.1007/s11837-019-03536-2

11. Zare, Y., Rhee, K.Y.: A simple model for electrical conductivity of polymer carbon nanotubes nanocomposites assuming the filler properties, interphase dimension, network level, interfacial tension and tunneling distance. Compos. Sci. Technol. **155**, 252–260 (2018). https://doi.org/10.1016/j.compscitech.2017.10.007

12. Zare, Y., Rhee, K.Y.: A simple methodology to predict the tunneling conductivity of polymer/CNT nanocomposites by the roles of tunneling distance, interphase and CNT waviness. RSC Adv. **7**(55), 34912–34921 (2017). https://doi.org/10.1039/c7ra04034b

13. Zare, Y., Rhee, K.Y.: Development of a conventional model to predict the electrical conductivity of polymer/carbon nanotubes nanocomposites by interphase, waviness and contact effects. Compos. Part A **100**, 305–312 (2017). https://doi.org/10.1016/j.compositesa.2017.05.031

14. Zare, Y., Garmabi, H., Rhee, K.Y.: Structural and phase separation characterization of poly(lactic acid)/poly(ethylene oxide)/carbon nanotube nanocomposites by rheological examinations. Compos. Part B **144**, 1–10 (2018). https://doi.org/10.1016/j.compositesb.2018.02.024

15. Mishra, K., Singh, R.P.: Effect of APTMS modification on multiwall carbon nanotube reinforced epoxy nanocomposites. Composites, Part B **162**, 425–432 (2019). https://doi.org/10.1016/j.compositesb.2018.12.134

16. Bakhtiary Davijani, A.A., Chang, H., Liu, H.C., Luo, J., Kumar, S.: Stress transfer in nanocomposites enabled by poly(methyl methacrylate) wrapping of carbon nanotubes. Polymer **130**, 191–198 (2017). https://doi.org/10.1016/j.polymer.2017.10.002

17. Arash, B., Wang, Q., Varadan, V.K.: Mechanical properties of carbon nanotube/polymer composites. Sci. Rep.-Uk. **4**, 6479 (2014). https://doi.org/10.1038/srep06479

18. Wang, S., Xin, F., Chen, Y., Qian, L., Chen, Y.: Phosphorus-nitrogen containing polymer wrapped carbon nanotubes and their flame-retardant effect on epoxy resin. Polym. Degrad. Stab. **129**, 133–141 (2016). https://doi.org/10.1016/j.polymdegradstab.2016.04.011

19. Zhang, J., Kong, Q., Wang, D.-Y.: Simultaneously improving the fire safety and mechanical properties of epoxy resin with Fe-CNTs via large-scale preparation. J. Mater. Chem. A. **6**(15), 6376–6386 (2018). https://doi.org/10.1039/c7ta10961j

20. Gkikas, G., Barkoula, N.M., Paipetis, A.S.: Effect of dispersion conditions on the thermo-mechanical and toughness properties of multi walled carbon nanotubes-reinforced epoxy. Compos. Part B **43**(6), 2697–2705 (2012). https://doi.org/10.1016/j.compositesb.2012.01.070

21. Zhang, J., Jiang, D.: Interconnected multi-walled carbon nanotubes reinforced polymer-matrix composites. Compos Sci Technol **71**(4), 466–470 (2011). https://doi.org/10.1016/j.compscitech.2010.12.020

22. Wang, D., Mu, X., Cai, W., Zhou, X., Song, L., Ma, C., Hu, Y.: Nano-bridge effects of carbon nanotubes on the properties reinforcement of two-dimensional molybdenum disulfide/polymer composites. Compos. Part A **121**, 36–44 (2019). https://doi.org/10.1016/j.compositesa.2019.03.011

23. Micheli, D., Vricella, A., Pastore, R., Delfini, A., Giusti, A., Albano, M., Marchetti, M., Moglie, F., Primiani, V.M.: Ballistic and electromagnetic shielding behaviour of multifunctional Kevlar fiber reinforced epoxy composites modified by carbon nanotubes. Carbon **104**, 141–156 (2016). https://doi.org/10.1016/j.carbon.2016.03.059

24. Ahmadi, M., Masoomi, M., Safi, S.: Mechanical property characterization of carbon nanofiber/epoxy nanocomposites reinforced by GMA-grafted UHMWPE fibers. Compos. Part B **83**, 43–49 (2015). https://doi.org/10.1016/j.compositesb.2015.08.006

25. Gouzman, I., Grossman, E., Verker, R., Atar, N., Bolker, A., Eliaz, N.: Advances in Polyimide-Based Materials for Space Applications. Adv. Mater. **31**(18), e1807738 (2019). https://doi.org/10.1002/adma.201807738

26. Park, S., Son, C.W., Lee, S., Kim, D.Y., Park, C., Eom, K.S., Fuller, T.F., Joh, H.-I., Jo, S.M.: Multicore-shell nanofiber architecture of polyimide/polyvinylidene fluoride blend for thermal and long-term stability of lithium ion battery separator. Sci. Rep-Uk. **6**, 36977 (2016). https://doi.org/10.1038/srep36977 https://www.nature.com/articles/srep36977#supplementary-information

27. Jiang, S., Uch, B., Agarwal, S., Greiner, A.: Ultralight, Thermally Insulating, Compressible Polyimide Fiber Assembled Sponges. ACS. Appl. Mater. Interfaces **9**(37), 32308–32315 (2017). https://doi.org/10.1021/acsami.7b11045

28. Yang, C., Dong, J., Fang, Y., Ma, L., Zhao, X., Zhang, Q.: Preparation of novel low-κ polyimide fibers with simultaneously excellent mechanical properties, UV-resistance and surface activity using chemically bonded hyperbranched polysiloxane. J. Mater. Chem. C. **6**(5), 1229–1238 (2018). https://doi.org/10.1039/C7TC05153K

29. Zhang, M., Niu, H., Wu, D.: Polyimide Fibers with High Strength and High Modulus: Preparation, Structures, Properties, and Applications. Macromol. Rapid. Commun. **39**(20), 1800141 (2018). https://doi.org/10.1002/marc.201800141

30. Eashoo, M., Shen, D., Wu, Z., Lee, C.J., Harris, F.W., Cheng, S.Z.D.: High-performance aromatic polyimide fibres: 2. Thermal mechanical and dynamic properties. Polymer **34**(15), 3209–3215 (1993). https://doi.org/10.1016/0032-3861(93)90392-N

31. Dong, J., Fang, Y., Gan, F., An, J., Zhao, X., Zhang, Q.: Enhanced mechanical properties of polyimide composite fibers containing amino functionalized carbon nanotubes. Compos. Sci. Technol. **135**, 137–145 (2016). https://doi.org/10.1016/j.compscitech.2016.09.021

32. Huang, J., Li, X., Luo, L., Wang, H., Wang, X., Li, K., Zhang, C., Liu, X.: Releasing silica-confined macromolecular crystallization to enhance mechanical properties of polyimide/silica hybrid fibers. Compos. Sci. Technol. **101**, 24–31 (2014). https://doi.org/10.1016/j.compscitech.2014.06.022

33. Wang, Y., Wang, W., Ding, X., Yu, D.: Multilayer-structured Ni-Co-Fe-P/polyaniline/polyimide composite fabric for robust electromagnetic shielding with low reflection characteristic. Chem. Eng. J. **380**, 122553 (2020). https://doi.org/10.1016/j.cej.2019.122553

34. Dong, J., Yang, C., Cheng, Y., Wu, T., Zhao, X., Zhang, Q.: Facile method for fabricating low dielectric constant polyimide fibers with hyperbranched polysiloxane. J. Mater. Chem. C. **5**(11), 2818–2825 (2017). https://doi.org/10.1039/C7TC00196G

35. Yang, T., Han, E., Wang, X., Wu, D.: Surface decoration of polyimide fiber with carbon nanotubes and its application for mechanical enhancement of phosphoric acid-based geopolymers. Appl. Surf. Sci. **416**, 200–212 (2017). https://doi.org/10.1016/j.apsusc.2017.04.166

36. Zhang, L., Han, E., Wu, Y., Wang, X., Wu, D.: Surface decoration of short-cut polyimide fibers with multi-walled carbon nanotubes and their application for reinforcement of lightweight PC/ABS composites. Appl. Surf. Sci. **442**, 124–137 (2018). https://doi.org/10.1016/j.apsusc.2018.02.129

37. Tian, G., Chen, B., Qi, S., Niu, H., Han, E., Wu, D.: Enhanced surface free energy of polyimide fibers by alkali treatment and its interfacial adhesion behavior to epoxy resins. Compos. Interfaces **23**(2), 145–155 (2016). https://doi.org/10.1080/09276440.2016.1112647

38. Owens, D.K., Wendt, R.C.: Estimation of the surface free energy of polymers. J. Appl. Polym. Sci. **13**(8), 1741–1747 (1969). https://doi.org/10.1002/app.1969.070130815

39. Bénard, Q., Fois, M., Grisel, M.: Roughness and fibre reinforcement effect onto wettability of composite surfaces. Appl. Surf. Sci. **253**(10), 4753–4758 (2007). https://doi.org/10.1016/j.apsusc.2006.10.049

40. Poulos, T.L.: Heme Enzyme Structure and Function. Chem. Rev. **114**(7), 3919–3962 (2014). https://doi.org/10.1021/cr400415k

41. Kong, M., Wang, K., Dong, R., Gao, H.: Enzyme catalytic nitration of aromatic compounds. Enzyme. Microb. Technol. **73–74**, 34–43 (2015). https://doi.org/10.1016/j.enzmictec.2015.03.008

42. Durand, A., Lalot, T., Brigodiot, M., Maréchal, E.: Enzyme-mediated initiation of acrylamide polymerization: reaction mechanism. Polymer **41**(23), 8183–8192 (2000). https://doi.org/10.1016/S0032-3861(00)00204-4

43. McKillop, A., Sanderson, W.R.: Sodium perborate and sodium percarbonate: Cheap, safe and versatile oxidising agents for organic synthesis. Tetrahedron **51**(22), 6145–6166 (1995). https://doi.org/10.1016/0040-4020(95)00304-Q

44. Li S, Gu A, Liang G, Yuan L, Xue J (2012) A facile and green preparation of poly(glycidyl methacrylate) coated aramide fibers. J. Mater. Chem. **22**(18). https://doi.org/10.1039/c2jm16602j

45. Zhang, T., Xu, X.L., Jin, Y.N., Wu, J., Xu, Z.K.: Immobilization of horseradish peroxidase (HRP) on polyimide nanofibers blending with carbon nanotubes. J. Mol. Catal. B: Enzym. **106**, 56–62 (2014). https://doi.org/10.1016/j.molcatb.2014.04.015

46. Lei, H., Zhang, M., Niu, H., Qi, S., Tian, G., Wu, D.: Multilevel structure analysis of polyimide fibers with different chemical constitutions. Polymer **149**, 96–105 (2018). https://doi.org/10.1016/j.polymer.2018.06.067

47. Park, C.Y., Kim, E.H., Kim, J.H., Lee, Y.M., Kim, J.H.: Novel semi-alicyclic polyimide membranes: Synthesis, characterization, and gas separation properties. Polymer **151**, 325–333 (2018). https://doi.org/10.1016/j.polymer.2018.07.052

48. Chang, Z., Xu, Y., Zhao, X., Zhang, Q., Chen, D.: Grafting Poly(methyl methacrylate) onto Polyimide Nanofibers via "Click" Reaction. ACS Appl Mater Interfaces **1**(12), 2804–2811 (2009). https://doi.org/10.1021/am900553k

49. Shi, Y., Belosinschi, D., Brouillette, F., Belfkira, A., Chabot, B.: Phosphorylation of Kraft fibers with phosphate esters. Carbohydr Polym **106**, 121–127 (2014). https://doi.org/10.1016/j.carbpol.2014.01.070

50. Puziy, A.M., Poddubnaya, O.I., Socha, R.P., Gurgul, J., Wisniewski, M.: XPS and NMR studies of phosphoric acid activated carbons. Carbon **46**(15), 2113–2123 (2008). https://doi.org/10.1016/j.carbon.2008.09.010

51. Wang, Y., Raman Pillai, S.K., Che, J., Chan-Park, M.B.: High Interlaminar Shear Strength Enhancement of Carbon Fiber/Epoxy Composite through Fiber- and Matrix-Anchored Carbon Nanotube Networks. ACS Appl Mater Interfaces **9**(10), 8960–8966 (2017). https://doi.org/10.1021/acsami.6b13197

52. Savas, L.A., Tayfun, U., Dogan, M.: The use of polyethylene copolymers as compatibilizers in carbon fiber reinforced high density polyethylene composites. Compos. Part B **99**, 188–195 (2016). https://doi.org/10.1016/j.compositesb.2016.06.043

53. Huda, M.S., Drzal, L.T., Mohanty, A.K., Misra, M.: Chopped glass and recycled newspaper as reinforcement fibers in injection molded poly(lactic acid) (PLA) composites: A comparative study. Compos. Sci. Technol. **66**(11), 1813–1824 (2006). https://doi.org/10.1016/j.compscitech.2005.10.015

54. Hu, C., Liao, X., Qin, Q.-H., Wang, G.: The fabrication and characterization of high density polyethylene composites reinforced by carbon nanotube coated carbon fibers. Compos. Part A **121**, 149–156 (2019). https://doi.org/10.1016/j.compositesa.2019.03.027

55. Sekhar, N.C., Varghese, L.A.: Mechanical, thermal, and rheological studies of phenolic resin modified with intercalated graphite prepared via liquid phase intercalation. Polym. Test. **79**, 106010 (2019). https://doi.org/10.1016/j.polymertesting.2019.106010

56. Gao, Y., Wang, Q., Wang, J., Huang, L., Yan, X., Zhang, X., He, Q., Xing, Z., Guo, Z.: Synthesis of Highly Efficient Flame Retardant High-Density Polyethylene Nanocomposites with Inorgano-Layered Double Hydroxides As Nanofiller Using Solvent Mixing Method. ACS. Appl. Mater. Interfaces. **6**(7), 5094–5104 (2014). https://doi.org/10.1021/am500265a

57. Zare, Y., Rhim, S., Garmabi, H., Rhee, K.Y.: A simple model for constant storage modulus of poly (lactic acid)/poly (ethylene oxide)/carbon nanotubes nanocomposites at low frequencies assuming the properties of interphase regions and networks. J. Mech. Behav. Biomed. Mater. **80**, 164–170 (2018). https://doi.org/10.1016/j.jmbbm.2018.01.037

58. Zare, Y., Rhee, K.Y.: Tensile strength prediction of carbon nanotube reinforced composites by expansion of cross-orthogonal skeleton structure. Compos. Part B **161**, 601–607 (2019). https://doi.org/10.1016/j.compositesb.2019.01.001

59. Zare, Y., Rhee, K.Y.: A power model to predict the electrical conductivity of CNT reinforced nanocomposites by considering interphase, networks and tunneling condition. Compos. Part B **155**, 11–18 (2018). https://doi.org/10.1016/j.compositesb.2018.08.028

60. Zare, Y.: An approach to study the roles of percolation threshold and interphase in tensile modulus of polymer/clay nanocomposites. J. Colloid. Interface. Sci. **486**, 249–254 (2017). https://doi.org/10.1016/j.jcis.2016.09.080

61. Zare, Y.: Modeling of tensile modulus in polymer/carbon nanotubes (CNT) nanocomposites. Synth. Met. **202**, 68–72 (2015). https://doi.org/10.1016/j.synthmet.2015.02.002

62. Li, H.X., Zare, Y., Rhee, K.Y.: The percolation threshold for tensile strength of polymer/CNT nanocomposites assuming filler network and interphase regions. Mater. Chem. Phys. **207**, 76–83 (2018). https://doi.org/10.1016/j.matchemphys.2017.12.053

Authors and Affiliations

Hongyang Dang[1] · Yunfeng Cao[2] · Ruqiang Zhang[1] · Zhu Long[1,3] · Shuai Guo[3] · Shihua Wang[3,4] · Zhiqiang Li[3,4]

[1]   Key Laboratory of Eco-Textiles, Ministry of Education, College of Textile Science and Engineering, Jiangnan University, Jiangsu Wuxi 214122, China

[2]   College of Light Industry and Food Science, Nanjing Forestry University, Nanjing 210037, China

[3]   Lianyungang Industrial Investment Group Co., Ltd, Jiangsu Lianyungang 222002, China

[4]   Lianyungang Fiber New Materials Research Institute Co., Ltd, Jiangsu Lianyungang 222002, China